Microconfined high-pressure transcritical fluid turbulence

ⓘD M. Bernades, ⓘD F. Capuano and ⓘD L. Jofre

COLLECTIONS

Note: This paper is part of the special topic, Multiphase flow in energy studies and applications: A special issue for MTCUE-2022.

EP This paper was selected as an Editor's Pick

View Online   Export Citation   CrossMark

ARTICLES YOU MAY BE INTERESTED IN

A new gas–liquid mass transfer enhancement method for a multi-downcomer sieve tray: Bubble breakup by falling droplets
Physics of Fluids 35, 013326 (2023); https://doi.org/10.1063/5.0131700

Effects of surface wettability on the aerodynamics of wind-driven droplets at the verge of shedding
Physics of Fluids 35, 017129 (2023); https://doi.org/10.1063/5.0128516

Unsteady self-similarity of jet fluid age and mass fraction
Physics of Fluids 35, 015139 (2023); https://doi.org/10.1063/5.0132042

Physics of Fluids

Special Topic: Paint and Coating Physics

Submit Today!

Microconfined high-pressure transcritical fluid turbulence 🔵EP

View Online   Export Citation   CrossMark

M. Bernades, 🆔 F. Capuano, 🆔 and L. Jofre[a] 🆔

AFFILIATIONS

Department of Fluid Mechanics, Universitat Politècnica de Catalunya·BarcelonaTech (UPC), Barcelona 08019, Spain

Note: This paper is part of the special topic, Multiphase flow in energy studies and applications: A special issue for MTCUE-2022.
[a]Author to whom correspondence should be addressed: lluis.jofre@upc.edu

ABSTRACT

Microfluidics technology has grown rapidly over the past decades due to its high surface-to-volume ratios, flow controllability, and length scales efficiently suited for interacting with microscopic elements. However, as a consequence of the small rates of mixing and transfer they achieve due to operating under laminar flow regimes, the utilization of microfluidics for energy applications has long been a key challenge. In this regard, as a result of the hydrodynamic and thermophysical properties they exhibit in the vicinity of the pseudo-boiling region, it has recently been proposed that microconfined turbulence could be achieved by operating at high-pressure transcritical fluid conditions. Nonetheless, the underlying flow mechanisms of such systems are still not well characterized, and, thus, need to be carefully investigated. This work, consequently, analyzes supercritical microconfined turbulence by computing direct numerical simulations of high-pressure $(P/P_c = 2)$ N_2 at transcritical conditions imposed by a temperature difference between the bottom $(T/T_c = 0.75)$ and top $(T/T_c = 1.5)$ walls for a friction Reynolds number of $Re_\tau = 100$ (bottom wall). The results obtained indicate that microconfined turbulence can be achieved under such conditions, leading to mixing and heat transfer increments up to $100\times$ and $20\times$, respectively, with respect to equivalent low-pressure systems. In addition, it is found that the near-wall flow physics deviates from a single-phase boundary layer theory due to the presence of a baroclinic instability in the vicinity of the hot/top wall. This instability is generated by the combination of the external force driving the flow and the large variation of density across the pseudo-boiling region, which strongly modifies the flow behavior in the vicinity of the wall and renders present "law of the wall" transformation models inaccurate.

I. INTRODUCTION

Standard microfluidic systems are typically limited to operate under laminar flow regimes due to their small characteristic hydraulic diameters $[D_h \sim 1–1000~\mu m]$ and bulk velocities $[u_b \sim \mathcal{O}(1)~m/s]$. In particular, at atmospheric pressure conditions, the Reynolds numbers encountered in microfluidics are in the order of $Re_b = u_b D_h/\nu \sim 0.1–100$, where $\nu \sim 10^{-6}–10^{-4}~m^2/s$ are typical values for the kinematic viscosity and consequently flows tend to remain laminar.[1] The smooth nature of this flow regime does not provide good mixing and transfer efficiencies in comparison to the performances obtained if turbulence, which is characterized by rapid fluctuations of flow variables in space and time, is present.[2] In this regard, an important body of research in microfluidics is focused on improving molecular diffusion in laminar flows through different strategies,[3] like, for example, fabricating serpentine-like microchannels. However, these techniques typically impose important construction complexities without exceptional increases in mixing and transfer rates. Other strategies significantly explored (i) try to achieve enhanced chaotic

mixing through electrokinetic forcing[4,5] or (ii) reach incipient turbulent flow conditions by extraordinarily increasing the volumetric flow rates (large sizes/velocities),[6–8] which is in contradiction to the small values typically sought in microfluidic applications. Finally, an interesting approach recently proposed to achieve turbulent regimes in microdevices is the utilization of flexible microfluidics.[9] However, this technology has not yet been demonstrated at the microscale since the experiments were performed utilizing microchannels with widths in the millimeter-scale range.

A novel potential approach to achieve microconfined turbulence, which is studied in this work, is based on operating under high-pressure supercritical conditions to leverage the hybrid thermophysical properties of supercritical fluids. High-pressure supercritical fluids are used in a wide range of engineering applications, like, for example, in gas turbines, supercritical water-cooled reactors, and liquid rocket engines.[10] They operate within high-pressure thermodynamic spaces in which intermolecular forces and finite packing volume effects become important. In this regard, it is important to distinguish

between supercritical gas-like and liquid-like fluids separated by the pseudo-boiling line:[11,12] (i) a supercritical liquid-like fluid is one whose density is large and whose transport coefficients behave similar to a liquid; whereas (ii) the density of supercritical gas-like fluids is smaller, and their transport coefficients vary similar to gases. In particular, the strategy proposed makes use of the rapid smooth transition when crossing the pseudo-boiling line to tune supercritical fluids to present liquid-like densities [$\rho \sim 10^3$ kg/m^3] and gas-like viscosities [$\mu \sim 10^{-5}$ Pa s], and therefore, achieve $Re_b \sim 10^3$–10^4 for typical microfluidic velocities and channel sizes, and favoring, in this manner, inertial over viscous forces and resulting in turbulent flow. Focusing on the thermophysical properties of different supercritical fluids, this approach has been recently explored by Bernades and Jofre.[1] The theoretical estimations presented in their work indicate that microconfined turbulent flow regimes can be potentially achieved by operating in the vicinity of the pseudo-boiling region for a wide range of popular working fluids, like, for example, carbon dioxide, methane, nitrogen, oxygen, and water. In connection with this strategy, Zhang et $al.$[13] explored mixing intensification for antisolvent processes by operating at high pressures in free-shear coflow configurations at isothermal conditions.[13] Nonetheless, the overall strategy is significantly different to the one studied in this work as (i) jet flows are inherently unstable, and consequently laminar-to-turbulent transition occurs in the range $Re_b \approx 30$–2000;[14] (ii) coflows require complex microfluidic configurations; and (iii) isothermal conditions are not generally suitable for energy-related applications.

The experimental study of supercritical fluids is notably challenging due to the high pressures typically involved, which significantly limit the quantity and quality of data that can be extracted from laboratory experiments and/or industrial applications.[15] This intricacy is further increased by the interest in working at microfluidics conditions. Consequently, this work will utilize computational approaches. In that sense, the inherent physics complexity of supercritical fluids across the pseudo-boiling region typically leads to poor prediction capabilities of Reynolds-averaged Navier–Stokes (RANS) simulation approaches.[10] Therefore, scale-resolving methodologies based on direct numerical simulation (DNS) and large eddy simulation (LES) are typically required to properly characterize and/or predict high-pressure transcritical turbulent flows. Selected examples of scale-resolving studies include (i) DNS of supercritical heat transfer in pipe flows by Bae et $al.$,[16,17] (ii) DNS of transcritical flows close to the critical point by Sengupta et $al.$,[18] (iii) LES and DNS of transcritical channel flows by Doehring and Adams[19] and Ma et $al.$,[20] respectively, and (iv) DNS of transcritical turbulent boundary layers by Kawai.[21] Nonetheless, scale-resolving computational studies of high-pressure transcritical flows are significantly challenging due to the appearance of spurious pressure oscillations and amplification of aliasing errors,[22] mostly as a result of the large density gradients across the pseudo-boiling region. In consequence, straightforward discretizations of the compressible equations of supercritical fluids motion typically turn out to be unsuitable. On this subject, the computational study presented in this work is based on a novel discretization approach grounded on extending a stable and non-dissipative formulation of the kinetic-energy preserving scheme introduced by Kennedy and Gruber[23] and later shown to be energy-preserving by Pirozzoli[24] and Coppola et $al.$[25] (referred to as KGP), to high-pressure transcritical flow problems.[26]

Therefore, the objectives of this study are to computationally (i) demonstrate the potential of supercritical fluids to achieve wall-bounded turbulent flow regimes at the microscale and (ii) characterize the corresponding flow physics. In this regard, the work is organized as follows. First, in Sec. II, the flow physics modeling of supercritical fluids is described together with the novel numerical scheme utilized. Next, the computational results are presented and analyzed in Sec. III. Finally, the work is concluded and future directions are proposed in Sec. IV.

II. PHYSICS MODELING AND NUMERICAL METHOD

The framework utilized for studying supercritical fluids turbulence in terms of (i) equations of fluid motion, (ii) real-gas thermodynamics, (iii) high-pressure transport coefficients, and (iv) numerical method is described below.

A. Equations of fluid motion

The turbulent flow motion of supercritical fluids is described by the following set of governing equations for mass, momentum, and pressure:

$$\frac{\partial \rho}{\partial t} + \nabla \cdot (\rho \mathbf{v}) = 0, \tag{1}$$

$$\frac{\partial (\rho \mathbf{v})}{\partial t} + \nabla \cdot (\rho \mathbf{v} \mathbf{v}) = -\nabla P + \nabla \cdot \boldsymbol{\tau}, \tag{2}$$

$$\frac{\partial P}{\partial t} + \mathbf{v} \cdot \nabla P + \rho c^2 \nabla \cdot \mathbf{v} = \frac{1}{\rho} \frac{\beta_v}{c_v \beta_T} (\boldsymbol{\tau} : \nabla \otimes \mathbf{v} - \nabla \cdot \boldsymbol{q}), \tag{3}$$

where ρ is the density, $\mathbf{v}$ is the velocity vector, P is the pressure, $\boldsymbol{\tau} = \mu(\nabla \mathbf{v} + \nabla \mathbf{v}^T) - (2\mu/3)(\nabla \cdot \mathbf{v})\boldsymbol{I}$ is the viscous stress tensor with μ as the dynamic viscosity and $\boldsymbol{I}$ as the identity matrix, $c = 1/\sqrt{\rho \beta_s}$ is the speed of sound with $\beta_s = -(1/v)(\partial v/\partial P)_s$ as the isentropic compressibility and $v = 1/\rho$ as the specific volume, $\beta_v = (1/v)(\partial v/\partial T)_P$ is the volume expansivity with T as the temperature, c_v is the isochoric specific heat capacity, $\beta_T = -(1/v)(\partial v/\partial P)_T$ is the isothermal compressibility, and $\boldsymbol{q} = -\kappa \nabla T$ is the Fourier heat conduction flux with κ as the thermal conductivity.

B. Real-gas thermodynamics

The thermodynamic space of solutions for the state variables pressure P, temperature T, and density ρ of a single substance is described by an equation of state. One popular choice for systems at high pressures, which is used in this study, is the Peng–Robinson[27] equation of state written as

$$P = \frac{R_u T}{\bar{v} - b} - \frac{a}{\bar{v}^2 + 2b\bar{v} - b^2}, \tag{4}$$

where R_u is the universal gas constant, $\bar{v} = W/\rho$ is the molar volume, and W is the molecular weight. The coefficients a and b take into account real-gas effects related to attractive forces and finite packing volume, respectively, and depend on the critical temperatures T_c, critical pressures P_c, and acentric factors ω. They are defined as

$$a = 0.457 \frac{(\mathrm{R}_u T_c)^2}{P_c} \left[1 + c \left(1 - \sqrt{T/T_c} \right) \right]^2, \tag{5}$$

$$b = 0.078 \frac{\mathrm{R}_u T_c}{P_c}, \tag{6}$$

where coefficient c is provided by

$$c = \begin{cases} 0.380 + 1.485\omega - 0.164\omega^2 + 0.017\omega^3 & \text{if } \omega > 0.49, \\ 0.375 + 1.542\omega - 0.270\omega^2 & \text{otherwise.} \end{cases}$$

The Peng–Robinson real-gas equation of state needs to be supplemented with the corresponding high-pressure thermodynamic variables based on departure functions[28] calculated as a difference between two states. In particular, their usefulness is to transform thermodynamic variables from ideal-gas conditions (low pressure—only temperature dependent) to supercritical conditions (high pressure). The ideal-gas parts are calculated by means of the NASA 7-coefficient polynomial,[29] while the analytical departure expressions to high pressures are derived from the Peng–Robinson equation of state as detailed in Jofre and Urzay.[12]

C. High-pressure transport coefficients

The high pressures involved in the analyses conducted in this work prevent the use of simple relations for the calculation of the dynamic viscosity μ and thermal conductivity κ. In this regard, standard methods for computing these coefficients for Newtonian fluids are based on the correlation expressions proposed by Chung et al.[30,31] These correlation expressions are mainly function of critical temperature T_c and density ρ_c, molecular weight W, acentric factor ω, association factor κ_a and dipole moment $\mathscr{M}$, and the NASA 7-coefficient polynomial;[29] further details can be found in dedicated works, like, for example, Poling et al.[32] and Jofre and Urzay.[12]

D. Numerical method

Simulations of high-pressure transcritical turbulence are strongly susceptible to numerical instabilities due to the presence of nonlinear thermodynamic phenomena and large density gradients, which can trigger spurious pressure oscillations that may contaminate the solution and even lead to its divergence. Consequently, it is highly beneficial that the numerical schemes utilized, in addition to being kinetic-energy preserving (KEP), attain the so-called pressure-equilibrium-preservation (PEP) property.[33,34] The numerical scheme utilized in this work has been developed specifically to be simultaneously KEP and PEP. The latter property is achieved by solving a pressure evolution equation. A thorough description and validation of this method can be found in Bernades et al.[26,35,36] In brief, the transport equations are numerically solved by adopting a standard semi-discretization procedure; viz., they are first discretized in space and then integrated in time. In particular, spatial operators are treated using second-order central-differencing schemes, and time-advancement is performed by means of a third-order strong-stability preserving (SSP) Runge–Kutta explicit approach.[37] The convective terms are expanded according to the Kennedy–Gruber–Pirozzoli (KGP) splitting,[25,38] which has been recently assessed for high-pressure supercritical fluids turbulence.[26] As a result, the method utilized (i) preserves kinetic energy by convection, (ii) is locally conservative for mass and momentum, (iii) preserves pressure equilibrium, and (iv) yields stable and robust numerical simulations without adding any numerical diffusion to the solution or stabilization procedures.

III. RESULTS AND DISCUSSION

Microconfined high-pressure transcritical turbulence is studied by means of DNS strategies based on the flow physics framework described in Sec. II. Data are obtained utilizing the in-house compressible flow solver RHEA.[39] The problem setup and discussion of results are described below.

A. Problem setup

The fluid selected to study and characterize microconfined high-pressure transcritical fluids turbulence is N_2, whose critical pressure and temperature are $P_c = 3.4$ MPa and $T_c = 126.2$ K. The fluid system is at a supercritical bulk pressure of $P_b/P_c = 2$ and confined between cold/bottom (cw) and hot/top (hw) isothermal walls, separated at a distance $H = 2\delta$ with $\delta = 100 \,\mu$m the channel half-height, at $T_{cw}/T_c = 0.75$ and $T_{hw}/T_c = 1.5$, respectively. Consequently, the boundary conditions imposed correspond to no-slip for the wall normal-direction and periodic for the streamwise and spanwise directions. This problem setup imposes the fluid to undergo a transcritical trajectory by operating within a thermodynamic region across the pseudo-boiling line. Based on preliminary theoretical estimations,[1] the friction Reynolds number selected at the cold/bottom wall is $Re_{\tau,cw} = \rho_{cw} u_{\tau,cw} \delta / \mu_{cw} = 100$, with $u_\tau = \sqrt{(\mu/\rho)(d\langle u \rangle/dy)}$ being the friction velocity, to ensure fully developed turbulent flow conditions; the ρ_{cw} and μ_{cw} values are obtained from the thermophysical model described in Sec. II. The mass flow rate in the streamwise direction is imposed through a body force controlled by a proportional feedback loop (gain $k_p = 0.1$) aimed at reducing the difference between the desired ($Re_{\tau,cw} = 100$) and measured (numerical) $Re_{\tau,cw}$ values. In addition, gravity forces are not considered as the resulting Froude number of the problem is $Fr = u_b / \sqrt{gH} \approx 55$, and consequently inertial forces are roughly $3000\times$ more important; viz., the importance of gravity scales as $1/Fr^2$.

The computational domain is $4\pi\delta \times 2\delta \times 4/3\pi\delta$ in the streamwise (x), wall-normal (y), and spanwise (z) directions, respectively, which is large enough to represent the largest flow scales of the problem.[40] The mesh resolution is selected based on preliminary studies. In particular, the monocomponent single-phase channel flow DNS performed by Chevalier et al.[41] at a same $Re_\tau = 100$ is considered as an initial reference. That study utilized $64 \times 64 \times 64$ grid points and corresponded to a fine-resolved DNS. For the problem of interest in this work, in addition to the classical consideration of the Kolmogorov scale, the length scales related to density gradients must also be considered. To this extent, based on the estimations provided by Jofre and Urzay,[11] the characteristic length scale for density gradients is approximately $10\times$ larger than the Kolmogorov scale, thereby confirming that the latter is the driving factor to select mesh resolution. Nonetheless, the mesh selected is $2\times$ finer in each direction with respect to Chevalier et al.[41] Consequently, this grid arrangement corresponds to a DNS of size $128 \times 128 \times 128$ grid points. The grid is uniform in the streamwise and spanwise directions with resolutions in wall units (based on cw values) equal to $\Delta x^+ \approx 9.8$ and $\Delta z^+ \approx 3.3$, and stretched toward the walls in the vertical direction with the first grid point at $y^+ = y u_{\tau,cw}/\nu_{cw} \approx 0.1$ and with sizes in the range $0.2 \lesssim \Delta y^+ \lesssim 2.3$, which are smaller than any of the reference DNS channel flow cases considered by Lee and Moser.[40]

The simulation strategy starts from a linear velocity profile with random fluctuations,[42] which is advanced in time to reach turbulent steady-state conditions after approximately five flow-through-time (FTT) units; based on the bulk velocity u_b and the length of the
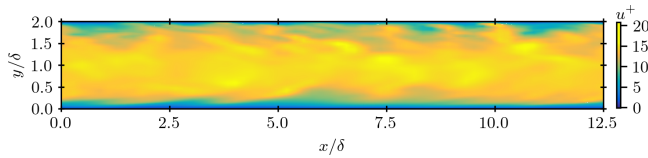
FIG. 1. Snapshot of instantaneous streamwise velocity in wall units u^+ on a x–y slice.

channel $L_x = 4\pi\delta$, a FTT is defined as $t_b = L_x/u_b \sim \delta/u_\tau$. In this regard, flow statistics are collected for roughly 10 FTTs once steady-state conditions are achieved. Finally, a snapshot of the instantaneous streamwise velocity in wall units u^+ on a x–y slice is displayed in Fig. 1 to provide qualitative information of the microconfined wall-bounded turbulence studied in this work.

B. Thermophysical analysis

The configuration of the problem, as previously introduced, forces the high-pressure fluid to undergo a second-order phase transition from supercritical liquid-like to supercritical gas-like by operating across the pseudo-boiling region. This phase transition is quantified in Fig. 2 by plotting the joint probability density function (PDF) of ensemble-averaged instantaneous values of reduced temperature T/T_c and density ρ/ρ_c together with the pseudo-boiling line (dashed–dotted curve). The results indicate that the most probable phase states correspond to supercritical liquid-like in the vicinity of the pseudo-boiling region ($T/T_c \approx 0.9$–1.1 and $\rho/\rho_c \approx 1$–2), followed by supercritical liquid-like at relatively cold temperatures (bottom wall region) and supercritical gas-like near the pseudo-boiling line, whereas supercritical gas-like states at relatively hot temperatures (top wall region) are significantly less probable. Consequently, at steady-state operating conditions, the system is dominated by supercritical liquid-like states near the pseudo-boiling line, which are characterized by densities similar to those of a liquid and presenting viscosities similar to a gas.[1] It can be also observed in the figure the rapid and smooth variation of
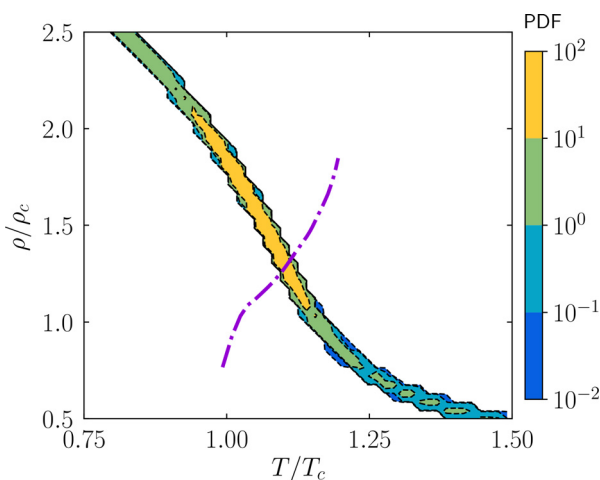

FIG. 2. Joint PDF of reduced temperature T/T_c and density ρ/ρ_c with the dashed–dotted curve indicating the pseudo-boiling line.
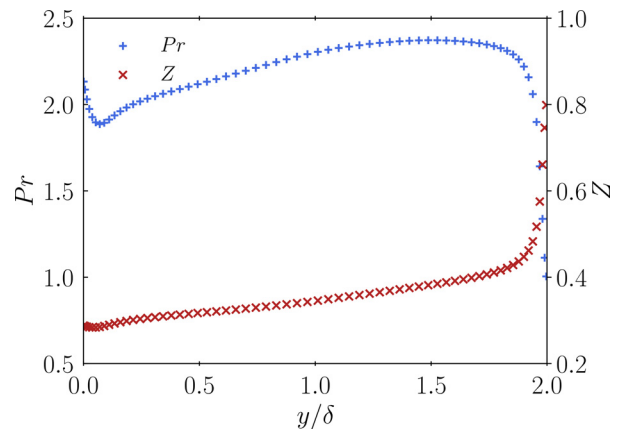

FIG. 3. Prandtl number Pr and compressibility factor Z along the wall-normal direction normalized by a channel half-height y/δ.

density (gradient) across the pseudo-boiling line along the transcritical temperature trajectory, which, as will be studied in the subsections below, induces a notably important baroclinic torque when combined with the external force moving the fluid.

The thermophysical properties, as depicted in Fig. 3, can be further characterized by analyzing the compressibility factor $Z = PW/(\rho R_u T)$ and Prandtl number $Pr = \mu c_P/\kappa$ along the wall-normal direction. It can be observed, focusing on Z, that the fluid behaves very differently from an ideal gas, i.e., $Z \neq 1$. In particular, the supercritical fluid markedly deviates toward low values ($Z \approx 0.3$) in the vicinity of the cold/bottom wall, which is indicative of large densities similar to those of a liquid. The Z values slightly increase monotonically, remaining below 0.5, when moving away from the cold wall up to $y/\delta \approx 1.9$. At that point, the curve rapidly increases to reach $Z \approx 0.8$ at the hot/top wall, which is still a value below 1 and corresponding to a relatively dense supercritical gas. The Prandtl number also depicts a very interesting behavior: (i) it presents values of $Pr \approx 2.2$ in the vicinity of the cold/bottom wall, indicating that momentum diffusivity dominates over thermal diffusivity, i.e., the momentum boundary layer is thicker than the thermal one; which is typical for liquid-like fluids; (ii) it rapidly reduces to values of approximately 1 close to the region of the hot/top wall as a result of crossing the pseudo-boiling line, denoting that momentum and thermal diffusivities are of the same importance; and (iii) it follows an oscillatory trajectory across the channel height with valley (cold/bottom side of the channel) and peak (hot/top side of the channel) values of $Pr \approx 1.9$ and $Pr \approx 2.4$, respectively. This behavior can be also observed from the instantaneous snapshot of Pr on a x-y plane shown in Fig. 4; note the relatively low values found in the vicinity of the walls (especially at the hot/top wall), and the higher values
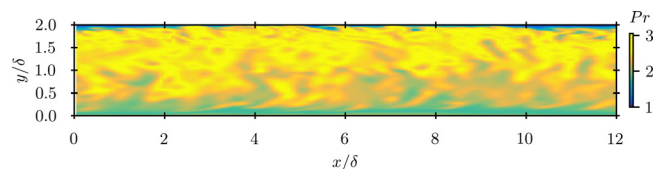

FIG. 4. Snapshot of instantaneous Prandtl number Pr on a x–y slice.

encountered in the center region. Consequently, in a bulk sense, momentum diffusivity is more important than thermal diffusivity; however, this difference rapidly reduces when approaching the hot/top wall.
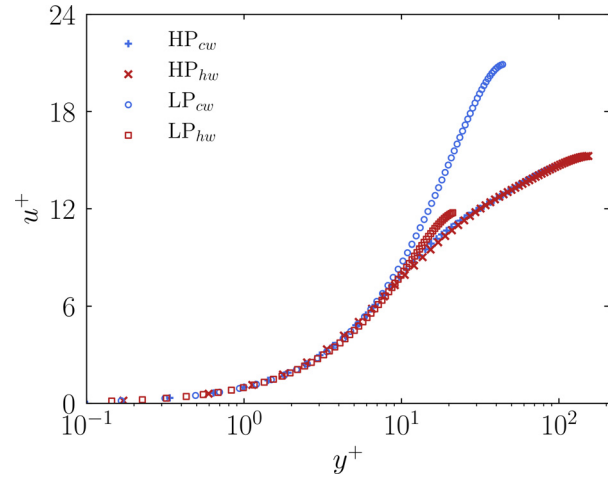
Finally, the values of friction Reynolds number Re_τ, skin-friction coefficient C_f, Prandtl number Pr, Nusselt number Nu, and Stanton number St obtained at the cold/bottom and hot/top walls are summarized in Table I, together with the quantities obtained for a similar system at low-pressure conditions. The low-pressure setup is defined by providing the same volumetric power input [i.e., $u_b(-dP/dx) = u_b(\tau_{w,cw} + \tau_{w,hw})/2\delta$ with τ_w denoting the wall-shear stress] to the fluid as in the high-pressure case to compare equivalent energized flows. In this regard, the mass flow rate in the streamwise direction is imposed through a body force controlled by a feedback loop, which in this case aims at reducing the difference between the desired and measured volumetric power input. However, the main difference is introduced by reducing the operating bulk pressure to $P_b/P_c = 0.03$. Therefore, a low-pressure framework is utilized based on the ideal-gas equation of state and Sutherland's law[43] for the dynamic viscosity and thermal conductivity, which are temperature-dependent in the following form:

$$\frac{\mu}{\mu_0} = \left(\frac{T}{T_0}\right)^{\frac{3}{2}} \frac{T_0 + S_\mu}{T + S_\mu} \quad \text{and} \quad \frac{\kappa}{\kappa_0} = \left(\frac{T}{T_0}\right)^{\frac{3}{2}} \frac{T_0 + S_\kappa}{T + S_\kappa}, \quad (7)$$

where μ_0 and κ_0 are evaluated at a reference temperature $T_0 = 273$ K, and $S_\mu = 107$ K and $S_\kappa = 150$ K are fitting parameters calibrated for N_2. It can be noted the five following observations. First, as characterized by the friction Reynolds number Re_τ, the high-pressure channel flow presents higher levels of inertia with respect to viscous forces at the hot/top wall in comparison to the cold/bottom wall, which, as will be analyzed in Subsection III C, corresponds to larger turbulent flow fluctuations. Instead, at low-pressure conditions, the flow becomes laminar as studied by Bernades and Jofre.[1] Second, the skin-friction coefficient C_f is an order of magnitude smaller at the top wall with respect to the bottom wall for the high-pressure case, while it is of the same order for the low-pressure system. Third, the Prandtl number Pr is approximately $2\times$ larger at the bottom wall at high pressures, and presents virtually no difference between walls at low pressure conditions. Fourth, the Nusselt number Nu, which quantifies the heat transfer enhancement by convection with respect to conduction, presents an increase in roughly $20\times$ for the supercritical system with respect to the low pressure case. Finally, for the high-pressure setup, the Stanton number St, which measures the ratio of heat transferred to a fluid with respect to its thermal capacity, at the top wall is an order of magnitude larger than at the bottom wall, while it presents similar values at low-pressure conditions. These results are very important as they
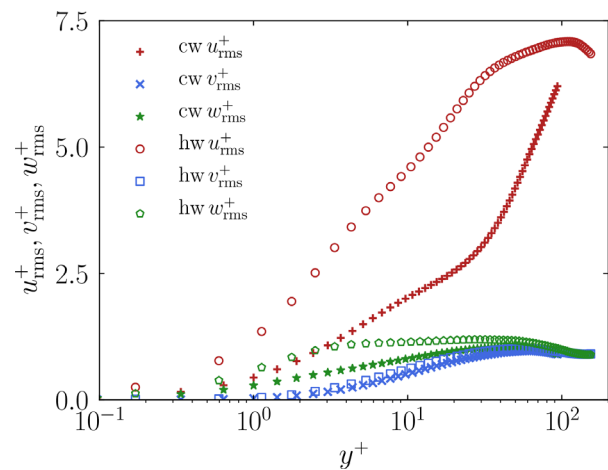

FIG. 5. Time-averaged streamwise velocity u^+ along the wall-normal direction y^+ for the high- (HP) and low-pressure (LP) cases at the cold (cw) and hot (hw) walls.

computationally corroborate the hypothesis that microconfined turbulent flow can be achieved when operating at high-pressure transcritical regimes, and consequently significantly larger values of flow mixing and heat transfer rates with respect to similar microchannels at atmospheric pressure conditions can be potentially obtained. For example, the size of the cooling systems of present-day microchips[44] could be significantly reduced (by a factor of $\mathcal{O}(10)$ as theoretically estimated by Bernades and Jofre[1]) using microfluidic channels at high-pressure supercritical fluid conditions.

C. Flow statistics

The time-averaged streamwise velocity u^+ and Favre-averaged root-mean-squared (rms) velocity fluctuations u_{rms}^+, v_{rms}^+ and w_{rms}^+ along the wall-normal direction y^+ in viscous units for the cold/bottom and hot/top walls are depicted in Figs. 5 and 6. It is important

TABLE I. Dimensionless numbers obtained from the high-pressure and low-pressure simulations at the cold/bottom and hot/top walls.

		Re_τ	C_f	Pr	Nu	St
High-pressure	Cold	100.0	0.020	2.14	5.61	0.026
	Hot	179.94	0.003	0.97	22.0	0.126
Low-pressure	Cold	49.17	0.014	0.78	1.37	0.036
	Hot	22.60	0.022	0.73	0.85	0.051

FIG. 6. Favre-averaged fluctuations of u^+, v^+, and w^+ along y^+ at the cold (cw) and hot (hw) walls for the high-pressure case.

to note that for the high-pressure results the maximum u^+ is located at $y/\delta = 1.07$ from the cold wall. Consequently, flow statistics are plotted from each wall to this particular position. Two main observations can be inferred from these plots. First, as shown in Fig. 5, the shapes of the time-averaged u^+ profiles for the high-pressure case present topologies similar to turbulent boundary layers, and collapse to the same curve for the two walls. Instead, at low-pressure conditions, the profiles present parabolic-like shapes reminiscent of laminar flow and with the line corresponding to the cold wall presenting larger velocity values toward the center. Second, focusing on the Favre-averaged rms velocity fluctuations for the high-pressure system shown in Fig. 6, turbulence intensity is significantly different between the hot/top (gas-like) and cold/bottom (liquid-like) walls in the streamwise direction. In particular, the hot wall presents larger fluctuations in the viscous sublayer and buffer region, while turbulence intensity grows following a concave parabola from the cold wall to the center of the channel. An equivalent, although significantly less pronounced, behavior is observed for the fluctuations in the spanwise direction, whereas they virtually collapse to the same curve for the wall-normal velocity.

The quantitative differences between the high-pressure and low-pressure cases discussed above can be undoubtedly visualized by examining the instantaneous snapshots of streamwise velocity shown in Fig. 7. From the figure, it can be easily observed the turbulent nature of the velocity field at high-pressure conditions, whereas the flow regime becomes laminar at low-pressure conditions. In particular, at high pressure, the flow presents a chaotic organization with a wide range of spatiotemporal scales characteristic of turbulence. Additionally, the boundary layer at the cold/bottom wall is relatively thicker than at the hot/top wall as it can be inferred from the size of
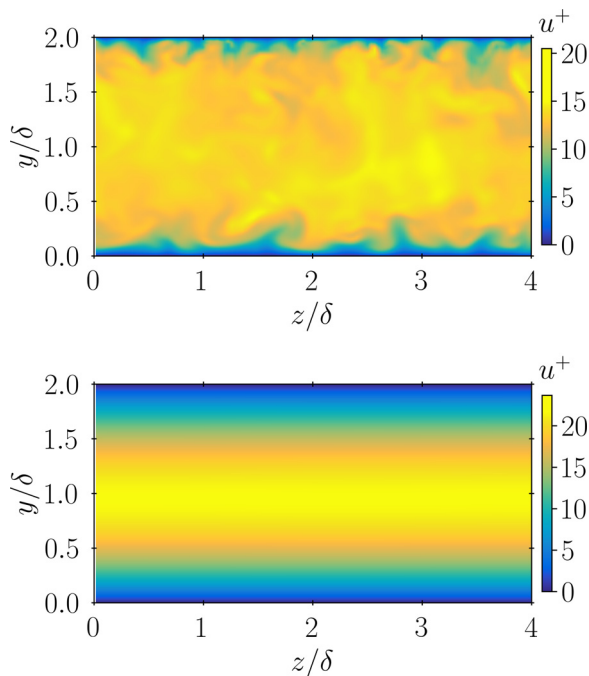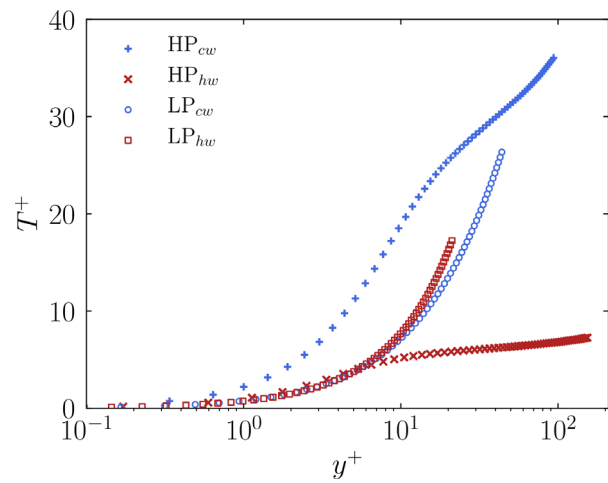

FIG. 8. Time-averaged temperature T^+ along the wall-normal direction y^+ for the high- (HP) and low-pressure (LP) cases at the cold (cw) and hot (hw) walls.

the flow structures emanating from both sides. However, as shown in Fig. 5, the two boundary layers virtually collapse to the same curve when they are normalized, respectively, by each wall friction velocity.

Focusing on the temperature distribution, different behaviors can be observed. In particular, Fig. 8 depicts the time-averaged temperature in viscous units $T^+ = (T - T_w)/T_\tau$, with T_w being the wall temperature and $T_\tau = [\kappa/(\rho c_P u_\tau)](d\langle T\rangle/dy)]$, along the wall-normal direction y^+, and Fig. 9 presents the Favre-averaged temperature fluctuations. As indicated by Fig. 8, the profiles collapse for the most part to a single curve for the low-pressure case, which is a consequence of the dominance of molecular diffusion over convective mixing resulting from the laminar regime developed. Instead, at high-pressure conditions, the time-averaged temperature values at the cold/bottom wall are roughly 2–4× larger than at the hot/top wall. This behavior is a direct consequence of the higher thermal inertia of the supercritical liquid-like fluid found at the cold/bottom part of the channel with
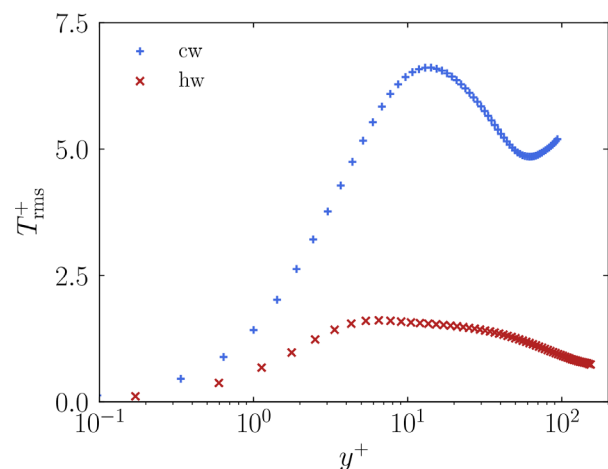

FIG. 7. Snapshots of instantaneous streamwise velocity u^+ on a y–z plane for high- (a) and low-pressure (b) cases.

FIG. 9. Favre-averaged fluctuations of T^+ along y^+ at the cold (cw) and hot (hw) walls for the high-pressure case.

respect to the supercritical gas-like fluid occupying the hot/top part. Additionally, as shown in Fig. 9, the temperature fluctuations are larger at the cold/bottom side of the channel in comparison to the hot/top region. Consequently, the degree of convective-dominated mixing is higher at the cold part, which enhances the transport of supercritical liquid-like fluid toward the hot side. In detail, the fluctuations at the hot/top wall follow a convex trajectory peaking at $y^+ \approx 50$ with the value $T^+ \approx 1.3$, whereas for the cold wall the fluctuations present a maximum of $T^+ \approx 6.3$ at $y^+ \approx 15$ followed by an oscillatory shape with a minimum of $T^+ \approx 5.0$ at $y^+ \approx 60$.

As depicted in Fig. 5, the streamwise velocity along the wall-normal direction roughly follows the topology of turbulent boundary layers. However, the inherent flow physics is significantly different from incompressible wall turbulence. In detail, as shown in Fig. 10, the u^+ profile as a function of y^+ does not exactly collapse to the standard "law of the wall" curve since, as initially proposed by van Driest[45] for non-isothermal regimes with variable density and viscosity, the variables need to be transformed accounting for the variation in mean quantities. However, as depicted in Fig. 10, the profile does not collapse either when utilizing an alternative transformation specifically suited for non-isothermal compressible boundary layers derived by Trettel and Larsson.[46] This transformation calculates y^+ and u^+ as

$$y^+ = \frac{\bar{\rho}}{\bar{\mu}} \sqrt{\frac{\tau_w}{\bar{\rho}}} y, \qquad (8)$$

$$u^+ = \int_0^{u^+} \sqrt{\frac{\bar{\rho}}{\rho_w}} \left[1 + \frac{1}{2\bar{\rho}} \frac{d\bar{\rho}}{dy} - \frac{1}{\bar{\mu}} \frac{d\bar{\mu}}{dy} y \right] du^+, \qquad (9)$$

where subindex ρ_w is the density at the walls, and $\bar{\rho}$ and $\bar{\mu}$ are mean quantities averaged over each y-plane. In particular, for both walls, the transformed results collapse to the standard profile along the viscous sublayer, but they deviate starting from the buffer layer especially for the hot/top wall. It is observed by performing inspectional analysis that the term dominating the time-averaged streamwise velocity in Eq. 9 is $\sqrt{\bar{\rho}/\rho_w}$. As a result, the significantly strong density variations across the channel largely influence the shape of the u^+ profiles. In

FIG. 10. Comparison of u^+ along y^+ against the "law of the wall" transformation by Trettel and Larsson[46] for the high-pressure case.

addition, due to the relatively small Reynolds numbers of the resulting turbulent flow, viscosity effects are still important which, since the transformation assumes that viscous stresses are negligible within the stress balance, further contribute to the deviation from the standard profile in the log-law region; especially at the hot/top wall where viscosity variation is the largest. Furthermore, the transformed friction Reynolds number[46] designed to incorporate the asymmetry of the solution in the wall-normal direction, which is defined as $Re_\tau^* = \rho^* u_\tau^* \delta^* / \mu^*$, where ρ^* and μ^* are evaluated at the y-position with maximum streamwise velocity, δ^* is the distance from the wall to this maximum position, and $u_\tau^* = \sqrt{\tau_w / \rho^*}$, correspond to $Re_\tau^* \approx 382$ and $Re_\tau^* \approx 132$ for the cold/bottom and hot/top walls, respectively. In particular, the transformed friction Reynolds number is used to compare a boundary layer with respect to the incompressible case at the same Re_τ value. Consequently, these values indicate that, as a result of the thermophysical and flow distribution along the wall-normal direction, the turbulent intensity is significantly larger at the cold/bottom wall with respect to the hot/top wall, which further supports the hypothesis that the large deviation from the standard "law of the wall" observed at the hot/top wall is caused by strong variations in density combined with the resulting relatively low friction Reynolds number achieved. Similarly, the recent data-driven transformation proposed by Volpiani et al.,[47] which was validated for a wide range of Reynolds and Mach numbers, has been also analyzed. However, the transformation has not been adequate for the this problem either. To this end, Subsection III D will investigate in more detail the underlying turbulent flow mechanisms responsible for the differences observed.

D. Turbulence sources

As previously introduced in Sec. III C, turbulent flow statistics differ substantially from the standard incompressible turbulent channel flow case. One of the underlying physical mechanisms responsible for such differences is the presence of a significantly localized baroclinic torque close to the hot/top wall. In particular, the torque, which is generated by the combination of (i) the external force driving the flow in the streamwise direction equivalent to an imposed pressure gradient of value $\nabla P = [-(\tau_{hw} + \tau_{cw})/2\delta, 0, 0]$, and (ii) the density gradient across the pseudo-boiling region in the wall-normal direction, is responsible for injecting vorticity with a peak value located in the vicinity of the hot/top wall as will be discussed below. As a result, notably higher levels of enstrophy are observed near the hot/top wall (values approximately $50\times$ larger) in comparison to the cold/bottom wall as quantified in Fig. 11. To further quantify this enhanced level of enstrophy especially near the hot/top wall, the high-pressure (HP) case is compared against the (i) low-pressure (LP) case defined in Sec. III B, and (ii) a low-pressure isothermal turbulent case at $Re_\tau = 100$ (LP isoT). This latter setup is similar to the LP case, but at an isothermal temperature of value $T/T_c = 0.75$ to achieve $Re_\tau = 100$ at both walls through the proportional controller. The enstrophy of this additional cases is also quantified in Fig. 11, indicating that the levels of kinetic energy corresponding to dissipation is significantly higher in the HP system with respect to the LP and LP isoT cases; especially in the region of the hot/top wall. In particular, the enstrophy levels near the hot/top wall for the HP case are roughly $100\times$ and $10\times$ larger than for LP and LP isoT, respectively, and these are responsible for altering the standard behavior of boundary layers as observed in Fig. 10.
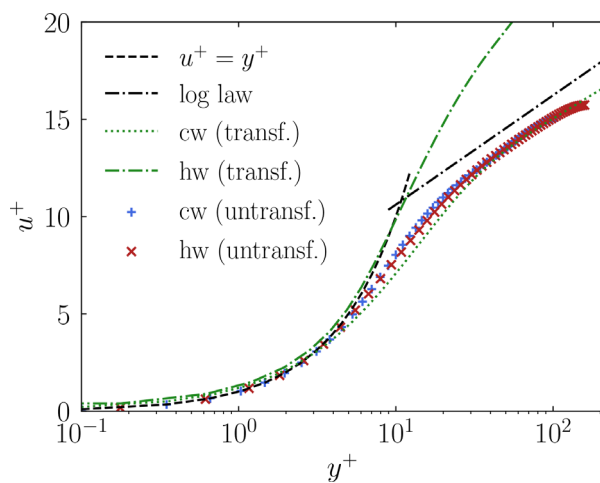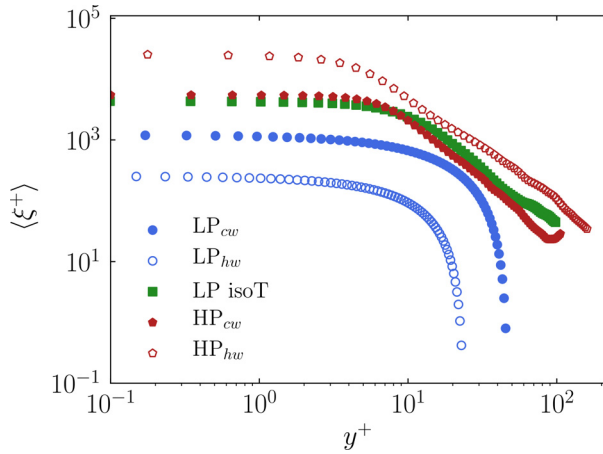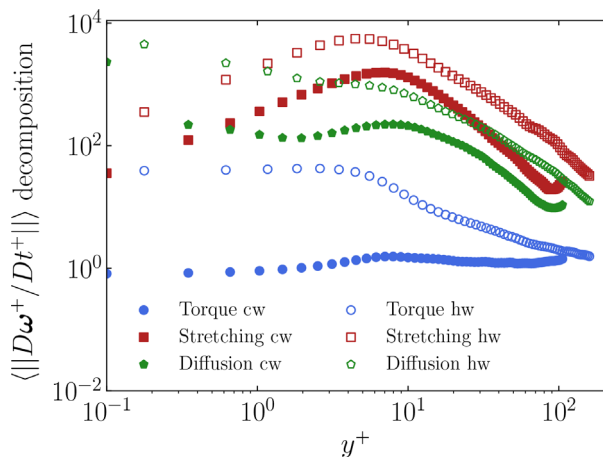
FIG. 11. Ensemble-averaged enstrophy values in wall units along the wall-normal direction for the low-pressure (LP), low-pressure at isothermal conditions (LP isoT), and high-pressure (HP) cases.

In order to characterize the intrinsic flow mechanisms responsible for this enhanced enstrophy levels, which can be linked to vorticity generation and distribution, the transport equation of vorticity is considered as follows:

$$\frac{\partial \boldsymbol{\omega}}{\partial t} + (\mathbf{v} \cdot \nabla)\boldsymbol{\omega} = (\boldsymbol{\omega} \cdot \nabla)\mathbf{v} - \boldsymbol{\omega}(\nabla \cdot \mathbf{v}) + \frac{1}{\rho^2}\nabla\rho$$
$$\times \nabla P + \nabla \times \left(\frac{1}{\rho}\nabla \cdot \boldsymbol{\tau}\right), \qquad (10)$$

where $\boldsymbol{\omega}$ is the vorticity, $(\boldsymbol{\omega} \cdot \nabla)\mathbf{v}$ and $-\boldsymbol{\omega}(\nabla \cdot \mathbf{v})$ represent, respectively, vortex stretching due to velocity gradients and compressibility effects, $1/\rho^2(\nabla\rho \times \nabla P)$ corresponds to the baroclinic torque, and $\nabla \times [(1/\rho)\nabla \cdot \boldsymbol{\tau}]$ is the vorticity diffusion term. In this regard, the different terms of the vorticity transport equation normalized by u_τ^2/δ^2
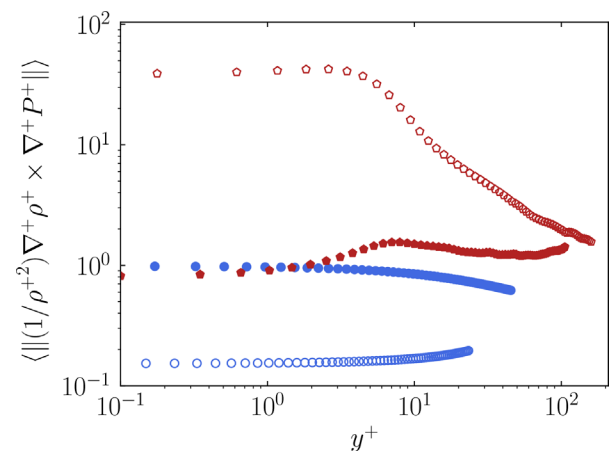

FIG. 12. Ensemble-averaged values of vortex stretching, baroclinic torque, and vorticity diffusion in wall units along the wall-normal direction for the high-pressure case.
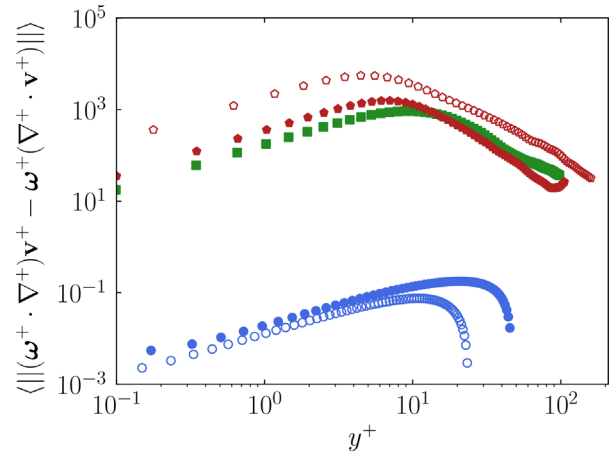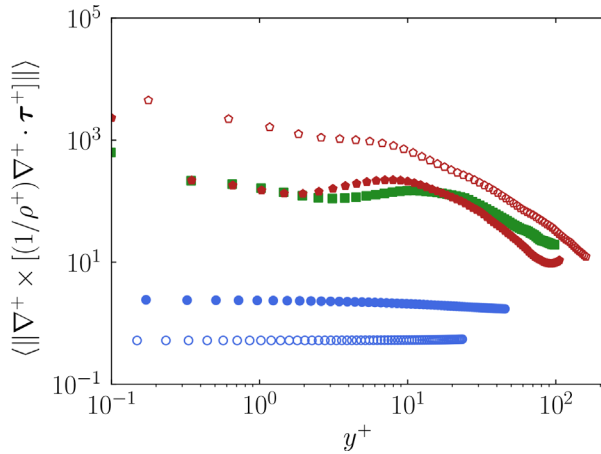

FIG. 13. Ensemble-averaged values of vortex stretching in wall units along the wall-normal direction for the low-pressure (LP), low-pressure at isothermal conditions (LP isoT), and high-pressure (HP) cases; the curve labels are defined in Fig. 11.

are shown in Fig. 12 for the cold/bottom and hot/top walls of the HP case based on ensemble-averaged values of 10 snapshots at different FTTs. It is observed from the figure that: (i) except for $y^+ \lesssim 1$ where viscosity effects are dominant, vortex stretching is larger than diffusion and baroclinic torque; and (ii) for each term, the values are larger at the hot/top wall than at the cold/bottom wall; especially for the baroclinic torque with a difference of roughly two orders of magnitude. These terms are additionally analyzed by comparing them against the LP and LP isoT levels in Figs. 13–15. The following observations can be inferred from the plots. First, as shown in Fig. 13, the levels of vortex stretching, which is characteristic of turbulent flows, for the cold/bottom wall of the HP case and LP isoT system are similar, presenting a maximum around the buffer layer, but they differ for the HP hot/top wall where the values are approximately $10\times$ larger. Instead, according to the laminar regime achieved, for the LP case, the vortex stretching

FIG. 14. Ensemble-averaged values of baroclinic torque in wall units along the wall-normal direction for the low-pressure (LP) and high-pressure (HP) cases; the curve labels are defined in Fig. 11.

FIG. 15. Ensemble-averaged values of vorticity diffusion in wall units along the wall-normal direction for the low-pressure (LP), low-pressure at isothermal conditions (LP isoT), and high-pressure (HP) cases; the curve labels are defined in Fig. 11.

FIG. 16. Ensemble-averaged values of velocity-gradient tensor discriminant in wall units along the wall-normal direction for the cold/bottom and hot/top walls of the high-pressure case.

values are four orders of magnitude smaller. Second, the baroclinic torque responsible for generating flow rotation, which is generated by the combination of the external force driving the flow and the variation of density, is negligible for the LP case as depicted in Fig. 14, but is significantly important (approximately $500\times$ larger) for the HP system as a result of the large density gradients obtained across the pseudo-boiling region. Third, these notable differences in terms of laminar/turbulent regime between HP and LP systems are further noted by the amount of vorticity dissipation shown in Fig. 15. As it can be observed from the figure, the vorticity dissipation is almost two orders of magnitude larger for the HP and LP isoT cases with respect to the LP case, which is indicative of the turbulent fluctuations present in the former systems and not present in the latter.

E. Small-scale flow topology

As discussed in Subsection III D, the baroclinic torque is the mechanism responsible for enhancing the flow rotation, whereas the vortex stretching acts as a turbulence generator by tilting and stretching the vortices. Hence, to further characterize the flow physics of the high-pressure system, the topology of the small scales is analyzed. In particular, the topological flow features are examined by considering the discriminant D_A of the velocity-gradient tensor $A_{ij} = \partial u_i / \partial x_j$ for compressible flows, which can be decomposed into symmetric S_{ij} (rate-of-strain) and skew-symmetric Ω_{ij} (rate-of-rotation) parts, and calculated as[48]

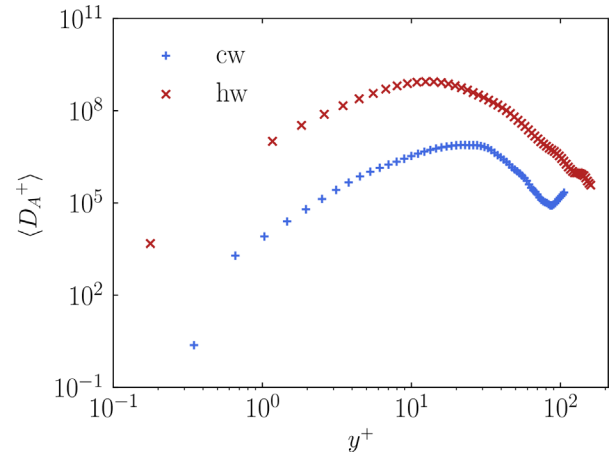$$D_A = 27 R_A^2 + (4 P_A^3 - 18 P_A Q_A) R_A + (4 Q_A^3 - P_A^2 Q_A^2), \quad (11)$$

where P_A, Q_A, and R_A are the first, second, and third invariants of the velocity-gradient tensor expressed as[49]

$$P_A = -\mathrm{tr}(A_{ij}) = -S_{ii}, \quad (12)$$

$$Q_A = \frac{1}{2}\left[\mathrm{tr}(A_{ij})^2 - \mathrm{tr}(A_{ij}^2)\right] = \frac{1}{2}(P_A^2 - S_{ij}S_{ji} - \Omega_{ij}\Omega_{ji}), \quad (13)$$

$$R_A = \frac{1}{2}\left[\mathrm{tr}(A_{ij})^3 + 3 P_A Q_A - \mathrm{tr}(A_{ij}^3)\right],$$
$$= \frac{1}{2}(-P_A^3 + 3 P_A Q_A - S_{ij}S_{jk}S_{ki} - 3\Omega_{ij}\Omega_{jk}S_{ki}). \quad (14)$$

In this regard, the ensemble-averaged values of normalized $D_A^+ = D_A(\delta/u_\tau)^6$ along the wall-normal direction for the cold/bottom and hot/top walls of the high-pressure case are shown in Fig. 16. As it can be observed, the discriminant presents larger positive values for the hot/top region (approximately $100\times$) with a maximum $D_A^+ \sim 10^9$ at $y^+ \approx 15$, whereas the maximum is at $y^+ \approx 30$ for the cold/bottom wall. Therefore, the flow is dominated by enstrophy along the entire channel, which is characteristic of turbulent flow systems. In more detail, Fig. 17 depicts the ensemble-averaged values of the three invariants in wall units along the wall-normal direction. The following observations can be obtained. First, P_A^+ is small and positive in the vicinity of the cold/bottom wall indicating that the flow tends to slightly expand, while it becomes large and negative near the hot/top wall corresponding to compression states in which the flow follows stable trajectories.[48] Second, Q_A^+, which measures the relative
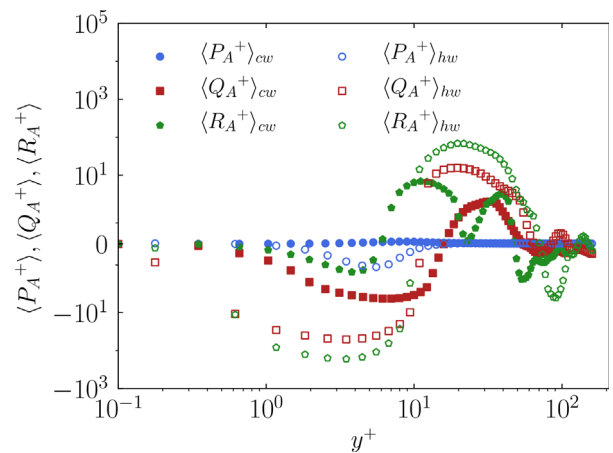
FIG. 17. Ensemble-averaged values of velocity-gradient tensor invariants in wall units along the wall-normal direction for the cold/bottom and hot/top walls of the high-pressure case.

importance of straining ($Q_A^+ < 0$) and rotational ($Q_A^+ > 0$) parts of the velocity-gradient tensor, fluctuates between negative and positive values for both walls, and presents a positive maximum around $y^+ \approx 20$–30. Hence, the flow is dominated by straining motions (especially for the hot/top wall) characterized by large rates of kinetic energy dissipation[50] close to the walls, whereas vorticity is prevalent toward the center of the channel. Similarly, R_A^+ also transitions from negative to positive values along the wall-normal direction for both walls. As a result, when moving slightly away from the walls, the flow tends to reverse direction from stable focus to unstable due to the dominance of vorticity in those regions.

IV. CONCLUSIONS

Direct numerical simulations have been performed to analyze and characterize the flow physics of microconfined high-pressure transcritical fluids turbulence. The problem of interest consists in a three-dimensional channel flow with (i) a friction Reynolds number of $Re_\tau = 100$ imposed at the cold/bottom wall, and (ii) a temperature difference between bottom and top walls to force the system cross the pseudo-boiling region. Such operating conditions result in turbulent flow at the microscale with a subsequent increase in fluid mixing and heat transfer. As it is studied and discussed, the achievement of turbulent flow is a result of the combination of (i) the thermophysical properties (relatively large density and small viscosity) of supercritical fluids across the pseudo-boiling region and (ii) the presence of a localized baroclinic torque close to the hot/top wall introducing vorticity into the system. To further characterize these effects, two additional cases at low-pressure (atmospheric) conditions have also been considered, which consist in a similar computational setup with same: (i) volumetric input power and (ii) same friction Reynolds number at isothermal conditions. The flow regime becomes laminar in the former case, whereas it remains turbulent (without heat transfer) in the latter.

The computational results demonstrate the feasibility of achieving microconfined turbulence by leveraging the properties of supercritical fluids. However, the resulting flow physics differs significantly from the typical behavior of turbulent boundary layers. Particularly, the first-order velocity statistics do not collapse to the standard "law of the wall" presenting the following features: (i) the hot/top wall deviates, especially in the log-law region, when transformed using non-isothermal models and (ii) the streamwise velocity fluctuations differ significantly between the cold/bottom and hot/top walls. In addition, the time-averaged temperature distribution also differs between walls, with the cold/bottom wall achieving slightly larger values due to the higher thermal inertia of supercritical liquid-like fluids. Moreover, the temperature fluctuations are higher at the cold/bottom wall as a result of the higher degree of convective mixing, which enhances the transport of supercritical liquid-like fluid toward the hot region. These differences between walls are mainly driven by a baroclinic torque localized in the vicinity of the hot/top wall, which is generated by the combination of the external force driving the flow in the streamwise direction and the density gradient across the pseudo-boiling region in the wall-normal direction, and yielding an increment of flow rotation in comparison to the isothermal low-pressure turbulent case also considered. As studied in detail, this baroclinic torque injects additional flow rotation into the system that is subsequently transformed into a wide range of scales (i.e., turbulent flow motions) through vortex stretching mechanisms. This behavior is further confirmed by the peak of velocity-gradient tensor discriminant in the vicinity of the hot/top wall, which is indicative of the prevalence of enstrophy over dissipation and characteristic of turbulent flow systems.

Finally, the rich phenomena of the results presented motivate the authors to continue studying the complex flow physics of microconfined turbulence at high-pressure transcritical conditions. Particularly, the focus in the short-term will be placed on (i) analyzing the flow behavior in the vicinity of the hot/top wall, especially in the log-law region where current non-isothermal transformation models fail; (ii) further characterizing the baroclinic torque identified; (iii) studying higher-order flow statistics for which the sensitivity to mesh resolution is currently unknown by the community; (iv) investigating the flow structures and patterns driving the enhanced mixing levels observed; and (v) expanding the knowledge of this problem by studying other fluids and operating conditions.

AUTHOR DECLARATIONS
Conflict of Interest

The authors have no conflicts to disclose.

Author Contributions

Marc Bernades: Conceptualization (lead); Formal analysis (lead); Investigation (lead); Methodology (lead); Writing – original draft (lead); Writing – review & editing (equal). **Francesco Capuano:** Supervision (supporting). **Lluís Jofre:** Funding acquisition (lead); Resources (lead); Supervision (lead); Writing – review & editing (equal).

DATA AVAILABILITY

The data that support the findings of this study are available from the corresponding author upon reasonable request.

REFERENCES

[1]M. Bernades and L. Jofre, "Thermophysical analysis of microconfined turbulent flow regimes at supercritical fluid conditions in heat transfer applications," J. Heat Transfer **144**, 082501 (2022).

[2]K. R. Sreenivasan, "Turbulent mixing: A perspective," Proc. Natl. Acad. Sci. **116**, 18175–18183 (2019).

[3]S. Hardt and F. Schönfeld, *Microfluidic Technologies for Miniaturized Analysis Systems*, 1st ed. (Springer, Cambridge, USA, 2007).

[4]G. R. Wang, F. Yang, and W. Zhao, "Microelectrokinetic turbulence in microfluidics at low Reynolds number," Phys. Rev. E. **93**, 013106 (2016).

[5]K. Nan, Z. Hu, W. Zhao, K. Wang, J. Bai, and G. Wang, "Large-scale flow in micro electrokinetic turbulent mixer," Micromachines **11**, 813 (2020).

[6]K. V. Sharp and R. J. Adrian, "Transition from laminar to turbulent flow in liquid filled microtubes," Exp. Fluids **36**, 741–747 (2004).

[7]W. Wibel and P. Ehrhard, "Experiments on the laminar/turbulent transition of liquid flows in rectangular microchannels," Heat Transfer Eng. **30**, 70–77 (2009).

[8]J. B. You, K. Kang, T. T. Tran, H. Park, W. R. Hwang, J. M. Kim, and S. G. Im, "PDMS-based turbulent microfluidic mixer," Lab Chip **15**, 1727 (2015).

[9]H. Fallahi, J. Zhang, H.-P. Phan, and N.-T. Nguyen, "Flexible microfluidics: Fundamentals, recent developments, and applications," Micromachines **10**, 830 (2019).

[10]J. Y. Yoo, "The turbulent flows of supercritical fluids with heat transfer," Annu. Rev. Fluid Mech. **45**, 495–525 (2013).

[11]L. Jofre and J. Urzay, "A characteristic length scale for density gradients in supercritical monocomponent flows near pseudoboiling," in *Annual Research Briefs* (Center for Turbulence Research, Stanford University, 2020), pp. 277–282.

[12]L. Jofre and J. Urzay, "Transcritical diffuse-interface hydrodynamics of propellants in high-pressure combustors of chemical propulsion systems," Prog. Energy Combust. Sci. **82**, 100877 (2021).

[13]F. Zhang, S. Marre, and A. Erriguible, "Mixing intensification under turbulent conditions in a high pressure microreactor," Chem. Eng. J. **382**, 122859 (2020).

[14]V. V. Lemanov, V. I. Terekhov, K. A. Sharov, and A. A. Shumeiko, "An experimental study of submerged jets at low Reynolds numbers," Tech. Phys. Lett. **39**, 421 (2013).

[15]X. Cheng and X. J. Liu, "Research challenges of heat transfer to supercritical fluids," J. Nucl. Rad. Sci. **4**, 011003 (2018).

[16]J. H. Bae, J. Y. Yoo, and H. Choi, "Direct numerical simulation of turbulent supercritical flows with heat transfer," Phys. Fluids **17**, 105104 (2005).

[17]J. H. Bae, J. Y. Yoo, and D. M. McEligot, "Direct numerical simulation of heated CO_2 flows at supercritical pressure in a vertical annulus at Re = 8900," Phys. Fluids **20**, 055108 (2008).

[18]U. Sengupta, H. Nemati, B. J. Boersma, and R. Pecnik, "Fully compressible low-Mach number simulations of carbon-dioxide at supercritical pressures and trans-critical temperatures," Flow Turbul. Combust. **99**, 909–931 (2017).

[19]A. Doehring, T. Kaller, S. J. Schmidt, and N. A. Adams, "Large-eddy simulation of turbulent channel flow at transcritical states," Int. J. Heat Fluid Flow **89**, 108781 (2021).

[20]P. C. Ma, X. I. A. Yang, and M. Ihme, "Structure of wall-bounded flows at transcritical conditions," Phys. Rev. Fluids **3**, 034609 (2018).

[21]S. Kawai, "Heated transcritical and unheated non-transcritical turbulent boundary layers at supercritical pressures," J. Fluid Mech. **865**, 563–601 (2019).

[22]P. C. Ma, Y. Lv, and M. Ihme, "An entropy-stable hybrid scheme for simulations of transcritical real-fluid flows," J. Comput. Phys. **340**, 330–357 (2017).

[23]C. A. Kennedy and A. Gruber, "Reduced aliasing formulations of the convective terms within the Navier–Stokes equations for a compressible fluid," J. Comput. Phys. **227**, 1676–1700 (2008).

[24]S. Pirozzoli, "Generalized conservative approximations of split convective derivative operators," J. Comput. Phys. **229**, 7180–7190 (2010).

[25]G. Coppola, F. Capuano, S. Pirozzoli, and L. de Luca, "Numerically stable formulations of convective terms for turbulent compressible flows," J. Comput. Phys. **382**, 86–104 (2019).

[26]M. Bernades, F. Capuano, F. X. Trias, and L. Jofre, "Energy-preserving stable computations of high-pressure supercritical fluids turbulence," in *9th European Congress on Computational Methods in Applied Sciences and Engineering (ECCOMAS)* (ECCOMAS, 2022), pp. 1–12.

[27]D. Y. Peng and D. B. Robinson, "A new two-constant equation of state," Ind. Eng. Chem. Fundam. **15**, 59–64 (1976).

[28]W. C. Reynolds and P. Colonna, *Thermodynamics: Fundamentals and Engineering Applications*, 1st ed. (Cambridge University Press, Cambridge, UK, 2019).

[29]A. Burcat and B. Ruscic, "Third millennium ideal gas and condensed phase thermochemical database for combustion with updates from active thermochemical tables," Technical Report (Argonne National Laboratory, 2005).

[30]T. H. Chung, L. L. Lee, and K. E. Starling, "Applications of kinetic gas theories and multiparameter correlation for prediction of dilute gas viscosity and thermal conductivity," Ind. Eng. Chem. Fundam. **23**, 8–13 (1984).

[31]T. H. Chung, M. Ajlan, L. L. Lee, and K. E. Starling, "Generalized multiparameter correlation for nonpolar and polar fluid transport properties," Ind. Eng. Chem. Fundam. **27**, 671–679 (1988).

[32]B. E. Poling, J. M. Prausnitz, and J. P. O'Connell, *Properties of Gases and Liquids*, 5th ed. (McGraw Hill, New York, USA, 2001).

[33]N. Shima, Y. Kuya, Y. Tamaki, and S. Kawai, "Preventing spurious pressure oscillations in split convective form discretization for compressible flows," J. Comput. Phys. **427**, 110060 (2021).

[34]G. Lacaze, T. Schmitt, A. Ruiz, and J. Oefelein, "Comparison of energy-,pressure- and enthalpy-based approaches for modeling supercritical flows," Comput. Fluids **181**, 35–56 (2019).

[35]M. Bernades, L. Jofre, and F. Capuano, "Investigation of a novel numerical scheme for high-pressure supercritical fluids turbulence," in *Proceedings of the Summer Program 2022* (Center for Turbulence Research, Stanford University, 2022), ctr.stanford.edu/proceedings-2022-summer-program.

[36]M. Bernades, L. Jofre, and F. Capuano, "Kinetic-energy- and pressure-equilibrium-preserving scheme for high-pressure supercritical fluids turbulence," J. Comput. Phys. (submitted) (2022).

[37]S. Gottlieb, C.-W. Shu, and E. Tadmor, "Strong stability-preserving high-order time discretization methods," SIAM Rev. **43**, 89–112 (2001).

[38]G. Coppola, F. Capuano, and L. de Luca, "Discrete energy-conservation properties in the numerical simulation of the Navier-Stokes equations," Appl. Mech. Rev. **71**, 010803 (2019).

[39]L. Jofre and G. Oyarzún, "RHEA—An open-source reproducible and hybrid-architecture flow solver Engineered for Academia," https://gitlab.com/ProjectRHEA/flowsolverrhea.

[40]M. Lee and R. D. Moser, "Direct numerical simulation of turbulent channel flow up to $Re_\tau \approx 5200$," J. Fluid Mech. **774**, 395–415 (2015).

[41]M. Chevalier, J. Hœpffner, T. R. Bewley, and D. S. Henningson, "State estimation in wall-bounded flow systems. Part 2. Turbulent flows," J. Fluid Mech. **552**, 167–187 (2006).

[42]K. S. Nelson and O. B. Fringer, "Reducing spin-up time for simulations of turbulent channel flow," Phys. Fluids **29**, 105101 (2017).

[43]W. Sutherland, "LII. the viscosity of gases and molecular force," London Edinburgh. Dublin Philos. Mag. J. Sci. **36**, 507–531 (1893).

[44]R. van Erp, R. Soleimanzadeh, L. Nela, G. Kampitsis, and E. Matioli, "Co-designing electronics with microfluidics for more sustainable cooling," Nature **585**, 211–216 (2020).

[45]E. R. van Driest, "Turbulent boundary layer in compressible fluids," J. Aeronaut. Sci. **18**, 145–1028 (1951).

[46]A. Trettel and J. Larsson, "Mean velocity scaling for compressible wall turbulence with heat transfer," Phys. Fluids **28**, 026102 (2016).

[47]P. S. Volpiani, P. S. Iyer, S. Pirozzoli, and J. Larsson, "Data-driven compressibility transformation for turbulent wall layers," Phys. Rev. Fluids **5**, 052602 (2020).

[48]S. Suman and S. S. Girimaji, "Velocity gradient invariants and local flow-field topology in compressible turbulence," J. Turbul. **11**, N2 (2010).

[49]M. Dodd and L. Jofre, "Small-scale flow topologies in decaying isotropic turbulence laden with finite-size droplets," Phys. Rev. Fluids **4**, 064303 (2019).

[50]J. Chen, M. Chong, J. Soria, R. Sondergaard, A. Perry, M. Rogers, R. Moser, and B. Cantwell, "A study of the topology of dissipating motions in direct numerical simulations of time-developing compressible and incompressible mixing layers," in *Proceedings of the Summer Program* (Center for Turbulence Research, Stanford University, 1990), pp. 139–161.